Development and adaptation of the Composite Rigid Body Algorithm and the Weak-Scatterer approach in view of the modeling of marine operations

P-Y Wuillaume[a,b], F. Rongère[a], A. Babarit[a], M. Philippe[b], P. Ferrant[a]

a. Ecole Centrale de Nantes, LHEEA - pierre-yves.wuillaume@ec-nantes.fr
b. INNOSEA

Résumé :

La simulation des opérations marines, en particulier des opérations de remontée ou de descente de colis, nécessite l'utilisation d'une théorie de dynamique multicorps pour les différents corps mis en jeu (bateau, câble et colis), d'une théorie hydrodynamique consistante et d'une modélisation des câbles. Ce papier présente une nouvelle approche pour simuler ce type d'opération basée sur le couplage entre une théorie multicorps et une théorie hydrodynamique.

La théorie multicorps utilise un formalisme issu de la robotique et un algorithme de dynamique directe adapté aux arbres cinématiques pour résoudre les équations de Newton-Euler. La modélisation des câbles suit le même procédé. La flexion et la torsion dans le câble ne sont pas prises en compte. Cette approche multicorps est comparée à la théorie câble dite « lumped mass ».

Les efforts hydrodynamiques sont calculés en supposant un fluide parfait et en faisant une hypothèse de type « weak-scatterer ». Cette hypothèse suppose que la composante perturbée du potentiel de vitesse du fluide est petite devant sa composante incidente et que les conditions limites de surface libre sont linéarisées par rapport à l'élévation de la surface libre incidente. Cet outil est couplé au solveur mécanique. Cette nouvelle stratégie de couplage est présentée dans ce papier.

Abstract:

The simulation of marine operations, in particular of lifting or lowering operations, requires the modeling of the whole system (ship, cable and payload) along with a theory of multibody dynamics, an appropriate hydrodynamic theory and cable's modeling. This paper presents a new approach to achieve this type of simulation based on a coupling between a multibody theory and a hydrodynamic one.

The multibody theory uses a robotics formalism and a direct dynamic algorithm based on recursive techniques for kinematic trees to solve the Newton-Euler equations. The cable modeling is based on the same multibody approach. There is neither bending nor torsion effect. This model is compared to the classical lumped mass theory.

Hydrodynamic loads are computed using a weakly nonlinear potential flow solver based on the weak-scatterer hypothesis. This approximation assumes the perturbation component of the fluid velocity potential is small compared to the incident one and the free surface boundary conditions are linearized with respect to the incident wave elevation. This solver is coupled with the mechanical one in order to perform the simulation. This new strategy to manage the coupling is presented in this paper.

Keywords: marine operations, coupling, weak-scatterer, multibody, cable

1 Introduction

With the development of the offshore wind industry, the simulation of the marine operations for the installation of wind turbines is required. This paper focuses on the operations of lowering and lifting of a payload. DNV published some norms in this field [1]. They are based on a simplified approach of the problem (characteristic quantities, regular design wave). Regarding the theory used in the commercial tools as Orcaflex [2] or Deeplines [3] for the modeling of the operations of lowering or lifting, they use a linear potential flow solver which assumes small amplitude motions of both the ship and the payload and cannot solve the unsteady hydrodynamic loads. But their multibody and cable solvers are consistent. On the other side, Hannan [4] developed a model based on a fully nonlinear potential flow solver but without an appropriate multibody or cable solver. The study presented in this paper wishes to have the best for the both approaches: an appropriate multibody/cable solver and a consistent hydrodynamic solver. To reach this objective, a weakly nonlinear potential flow solver is coupled with a multibody mechanical solver. Doing so, the long term goal is to quantify the interest of using this hydrodynamic solver in this kind of marine operation.

2 Multibody theory

The multibody offshore numerical tool used in this paper is InWave [5] developed by Innosea and Ecole Centrale de Nantes. It performs time domain simulations of kinematic trees in using a direct dynamics algorithm to solve the Newton-Euler equations. A kinematic tree is a set of interconnected bodies where each body has only one ancestor and potentially several successors. The base body (the only one without ancestor) of the multibody system is floating in six degrees of freedom (*dof*). Between a body (except the base) and its ancestor, there is a joint, revolute or prismatic, granting for a single degree of freedom. This multibody approach uses relative coordinates and is parameterized using the modified Denavit-Hartenberg parameters [6].

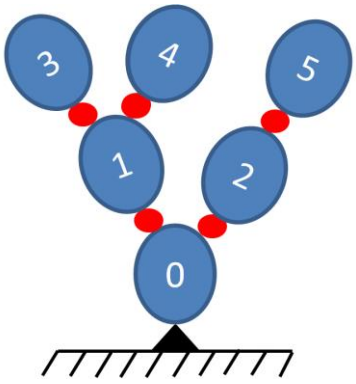

Figure 1: Kinematic tree (blue = bodies, red = joints)

The Lagrangian formulation of the Newton-Euler equations to solve is:

$$\begin{pmatrix} \mathbf{0}_{6\times 1} \\ \boldsymbol{\Gamma} \end{pmatrix} = \boldsymbol{H} \begin{pmatrix} {}^{0}\dot{\boldsymbol{V}}_{0} \\ \ddot{\boldsymbol{q}} \end{pmatrix} + \boldsymbol{C} \tag{1}$$

Where $\boldsymbol{\Gamma}$ is the vector of the torques (or forces) around (or along) the revolute (or prismatic) joints, $\boldsymbol{H} = \begin{pmatrix} \boldsymbol{H_{11}} & \boldsymbol{H_{12}} \\ \boldsymbol{H_{21}} & \boldsymbol{H_{22}} \end{pmatrix}$ the generalized inertia matrix, $\boldsymbol{C} = \begin{pmatrix} \boldsymbol{C_1} \\ \boldsymbol{C_2} \end{pmatrix}$ the vector of the inertia and external forces, ${}^{\mathbf{0}}\dot{\boldsymbol{V}}_{\mathbf{0}}$ is the acceleration of the floating base expressed in its own frame and $\ddot{\boldsymbol{q}}$ the articular acceleration of each joint. By definition, a direct dynamics algorithm means $\boldsymbol{\Gamma}$, $\boldsymbol{C}$ and $\boldsymbol{H}$ are known whereas ${}^{\mathbf{0}}\dot{\boldsymbol{V}}_{\mathbf{0}}$ and $\ddot{\boldsymbol{q}}$ are unknown.

The size of the system is the number of joints plus the *dof* of the base. The state vector is:

$$\boldsymbol{Y} = [\boldsymbol{\eta}^T \ \boldsymbol{\nu}^T \ \boldsymbol{q}^T \ \dot{\boldsymbol{q}}^T]^T \tag{2}$$

Where $\boldsymbol{\eta}$ is the position of the base in the inertial frame, $\boldsymbol{\nu}$ is the velocity of the base with respect to the inertial frame and expressed in the frame of the base, $\boldsymbol{q}$ is the vector of the articular positions and $\dot{\boldsymbol{q}}$ is the vector of the articular velocities.

Rongère [7] presented a first approach to simulate the offshore structures and solve the equation (1). The algorithm presented in [7] was similar to the Articulated Body Algorithm of Featherstone [8]. The inversion of the matrix $\boldsymbol{H}$ was not required. An extension of this work was made by Rongère [9] to take into account the hydrodynamic interactions in using the Composite Rigid Body Algorithm [8]. This modification involves the inversion of $\boldsymbol{H}$ and is more suitable to deal with the linear hydrodynamic added mass coefficients. The following notations come from [7].

The first main step of this latter algorithm is the computation of the following kinematic and dynamic quantities for each body *j*:

- Transformation matrices ${}^j\boldsymbol{T}_i$;
- Velocities in the body frames;
- Coriolis accelerations ${}^j\boldsymbol{\gamma}_j$;
- External loads and centrifugal effects ${}^j\boldsymbol{\beta}_j$.

The motion equation of the system made of the body *j* and all its successors (which therefore has no successor) is:

$${}^j\boldsymbol{F}_j = {}^j\boldsymbol{m}_j^c \, {}^j\dot{\boldsymbol{V}}_j + {}^j\boldsymbol{\beta}_j^c \tag{3}$$

Where ${}^j\boldsymbol{m}_j^c$ and ${}^j\boldsymbol{\beta}_j^c$ are the generalized mass matrix and the generalized load vector of the composite body *j*. ${}^j\boldsymbol{F}_j$ is the internal force and moment across the joint *j*, connecting the body *j* and its unique ancestor. ${}^j\dot{\boldsymbol{V}}_j$ is the acceleration of the body *j* expressed in its frame.
The aim of the second main step is the computation for each body of ${}^j\boldsymbol{m}_j^c$ and ${}^j\boldsymbol{\beta}_j^c$:

$$\begin{aligned} {}^j\boldsymbol{m}_j^c &= {}^j\boldsymbol{m}_j + \sum_{k \,/\, a(k)=j} {}^k\boldsymbol{T}_j^T \, {}^k\boldsymbol{m}_k^c \, {}^k\boldsymbol{T}_j \\ {}^j\boldsymbol{\beta}_j^c &= {}^j\boldsymbol{\beta}_j + \sum_{k \,/\, a(k)=j} {}^k\boldsymbol{T}_j^T [{}^k\boldsymbol{m}_k^c \, {}^k\boldsymbol{\gamma}_k + {}^k\boldsymbol{\beta}_k^c] \end{aligned} \tag{4}$$

Finally, the last step is to build of the matrix $\boldsymbol{H}$ and the vector $\boldsymbol{C}$. The vector $\boldsymbol{\Gamma}$ depends on the type of the internal loads which are required in the multibody system.

The generalized inertia matrix $\boldsymbol{H}$ is defined by:

$$\begin{aligned} \boldsymbol{H_{11}} &= {}^0\boldsymbol{m}_0^c \\ col_k(\boldsymbol{H_{12}}) &= {}^k\boldsymbol{T}_0^T \, {}^k\boldsymbol{m}_k^c \, {}^k\boldsymbol{a}_k \ for \ k \in [|1, n|] \\ \boldsymbol{H_{21}} &= \boldsymbol{H_{12}}^T \\ row_j\big(col_k(\boldsymbol{H_{22}})\big) &= {}^j\boldsymbol{a}_j^T \, {}^j\boldsymbol{m}_j^c \, {}^j\boldsymbol{T}_k^T \, {}^k\boldsymbol{a}_k \ \ for \ (j,k) \in [|1, n|]^2 \ such \ as \ k \geq j \end{aligned} \tag{5}$$

And the vector $\boldsymbol{C}$ is defined by:

$$\boldsymbol{C_1} = {}^0\boldsymbol{\beta}_0 + \sum_{k=1}^{n} {}^k\boldsymbol{T}_0^T \big({}^k\boldsymbol{\beta}_k + {}^k\boldsymbol{m}_k^c \, {}^k\boldsymbol{\gamma}_k\big) \tag{6}$$

$$row_j(\boldsymbol{C_2}) = {}^j\boldsymbol{a}_j^T \left({}^j\boldsymbol{m}_j^c \sum_{k=0}^{j} {}^j\boldsymbol{T}_k \, {}^k\boldsymbol{\gamma}_k + {}^j\boldsymbol{\beta}_j^c \big|_{\ddot{\boldsymbol{q}}=0_{n\times 1}} \right) for\ j \in [|1,n|]$$

Where n is the number of joints and ${}^j\boldsymbol{a}_j$ the axis of the joint j expressed in the body j's frame.
Finally the acceleration can be computed by the inversion of the matrix $\boldsymbol{H}$ and the state vector time-stepped in using a RK4 scheme.

3 Cable modeling using a multibody theory

In an operation of lifting or lowering, a cable is necessary. Several cable libraries are available (Map++ [10], MoorDyn [11], etc.). It is easier to use InWave in order to simulate cables rather than using an external program which would not be well adapted to the multibody formalism presented in 2. Consequently we want to compare the cable modeling obtained with a multibody approach to a classically cable theory in order to validate this approach. Masciola [12] did a survey of the different time-domain cable theories which are commonly used: lumped mass model (low and high order), finite-element model and finite-difference model. In another paper, Masciola [13] presented the quasi-static theory. A simple but consistent cable model to compare with is to use a low-order lumped mass theory. Indeed firstly the quasi-static theory neglects the dynamical effects and secondly in a lowering/lifting operation the cable stays mainly vertical so the effect of bending and torsion effects are not predominant.
The details of the low order lumped mass model can be found in [14] and [15].

In the low order lumped mass model, a cable is discretized into massless points. Each point has three degree of freedom. To match this description, the multibody theory requires three bodies (of which two are massless) to ensure the three degrees of freedom. Thus three joints are used: two revolutes and one prismatic. Internal loads are also present in the lumped mass model with axial tension and axial damping. For a cable element j, the components of the vector $\boldsymbol{\Gamma}$ of the internal loads become:

$$\begin{aligned} \Gamma_{3j-2} &= 0 \\ \Gamma_{3j-1} &= 0 \\ \Gamma_{3j} &= \begin{cases} -\frac{EA}{Lu}\left(q_{3j} + Lu\right) - \frac{CA}{Lu}\dot{q}_{3j}, & \left|q_{3j}\right| \geq Lu \\ -\frac{CA}{Lu}\dot{q}_{3j}, & \left|q_{3j}\right| < Lu \end{cases} \end{aligned} \tag{7}$$

Where Γ_{3j-2} is the internal load of the first revolute joint, $\Gamma_{3j-1}$of the second one and Γ_{3j} of the prismatic joint. Lu is the unstretched length, E the Young modulus, A the area of the section, C the damping coefficient, q_{3j} the size of the cable element and $\dot{q}_{3j}$ the axial velocity. It is assumed there is no compression which explained the condition on q_{3j}.

The two approaches (multibody and low-order lumped mass) are used to model a cable of three elements.
The following table summarizes the cable characteristics of the test case.

Linear density $(kg.m^{-1})$	100
Diameter (m)	0.0332
Young modulus (Pa)	7.75e7
Damping coefficient $(N.s.m^{-1})$	1e5
Unstretched length (m)	10
Position of the upper node (m)	(0.0 ; 0.0 ; 20)
Position of lower node (m)	(-2.0 ; 0.0 ; 10)

Table 1: Cable characteristics

The time step is 0.001 s and the duration of the simulation is 10 s.

The figure 2 presents the length of the third cable element for the two models.

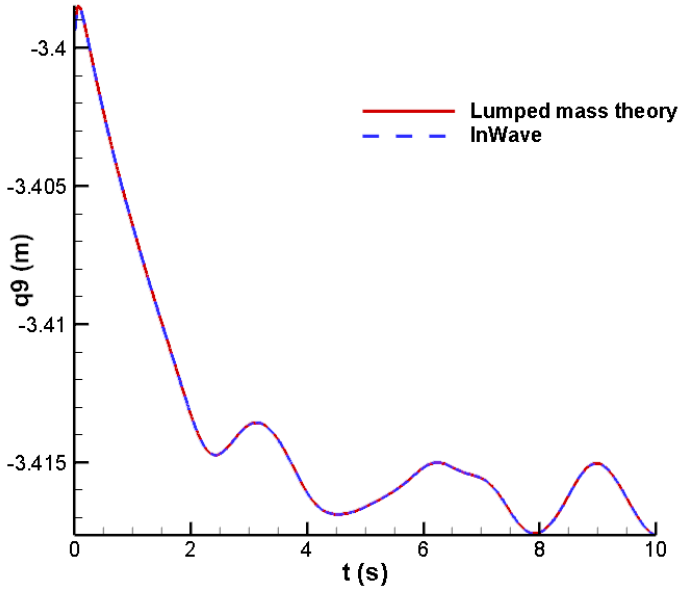

Figure 2: Length of the third cable element in using a low order lumped mass theory (red) and InWave (bleu)

Hence the two approaches give the same results, but not with the same CPU time. A lumped mass model has only one loop over the cable elements whereas the multibody theory has three loops over the multibody system. Moreover, three bodies are necessary to model a cable element. Consequently the multibody approach is more time-consuming than the low-order lumped mass model. A way to speed up the multibody approach is to walk along the number of cable elements instead of the number of bodies. The multibody equations previously presented have to be solved three at a time.

Equation (4), (5) and (6) become:

$$
\begin{aligned}
{}^{3(j-1)}\boldsymbol{m}^{c}_{3(j-1)} &= {}^{3(j-1)}\boldsymbol{m}_{3(j-1)} + {}^{3j}\boldsymbol{T}^{T}_{3(j-1)}\,{}^{3j}\boldsymbol{m}^{c}_{3j}\,{}^{3j}\boldsymbol{T}_{3(j-1)} \\
{}^{3(j-1)}\boldsymbol{\beta}^{c}_{3(j-1)} &= {}^{3(j-1)}\boldsymbol{\beta}_{3(j-1)} + {}^{3j}\boldsymbol{T}^{T}_{3(j-1)}\left[{}^{3j}\boldsymbol{m}^{c}_{3j}\left({}^{3j}T_{3j-2}\,{}^{3j-2}\boldsymbol{\gamma}_{3j-2} + {}^{3j}\boldsymbol{T}_{3j-1}\,{}^{3j-1}\boldsymbol{\gamma}_{3j-1} + {}^{3j}\boldsymbol{\gamma}_{3j}\right) + {}^{3j}\boldsymbol{\beta}^{c}_{3j}\right]
\end{aligned}
\tag{8}
$$

$$
\boldsymbol{H_{11}} = {}^{0}\boldsymbol{m}^{c}_{0} \tag{9}
$$

$$col_{[3k-2,3k-1,3k]}(\boldsymbol{H}_{12}) = {}^{3k}\boldsymbol{T}_0^T\,{}^{3k}\boldsymbol{m}_{3k}^c\boldsymbol{P}_k \; for\; k \in [|1, N_{elements}|]$$

$$\boldsymbol{H_{21}} = \boldsymbol{H_{12}^T}$$

$$row_{[3j-2,3j-1,3j]}\left(col_{[3k-2,3k-1,3k]}(\boldsymbol{H_{22}})\right) = \boldsymbol{P}_j^T\,{}^{3j}\boldsymbol{m}_{3j}^c\,{}^{3j}\boldsymbol{T}_{3k}^T\boldsymbol{P}_k \;\; for\; (j,k) \in [|1, N_{elements}|]^2 \; such\; as\; k \geq j$$

$$\boldsymbol{C_1} = {}^0\boldsymbol{\beta}_0 + \sum_{k=1}^{n} {}^k\boldsymbol{T}_0^T({}^k\boldsymbol{\beta}_k + {}^k\boldsymbol{m}_k^c\,{}^k\boldsymbol{\gamma}_k)$$

$$row_{[3j-2,3j-1,3j]}(\boldsymbol{C_2}) = \boldsymbol{P}_j^T\left({}^{3j}\boldsymbol{m}_{3j}^c\sum_{k=0}^{j}{}^{3j}\boldsymbol{T}_{3k}({}^{3k}\boldsymbol{T}_{3k-2}\,{}^{3k-2}\boldsymbol{\gamma}_{3k-2} + {}^{3k}\boldsymbol{T}_{3k-1}\,{}^{3k-1}\boldsymbol{\gamma}_{3k-1} + {}^{3k}\boldsymbol{\gamma}_{3k}) + {}^{3j}\boldsymbol{\beta}_{3j}^c\right) for\; j \in [|1, N_{elements}|] \quad (10)$$

Where $\boldsymbol{P}_j$ is a 6×3 matrix:

$$\boldsymbol{P}_j = \begin{pmatrix} {}^{3j}\boldsymbol{T}_{3j-2}\,{}^{3j-2}\boldsymbol{a}_{3j-2} & {}^{3j}\boldsymbol{T}_{3j-1}\,{}^{3j-1}\boldsymbol{a}_{3j-1} & {}^{3j}\boldsymbol{a}_{3j} \end{pmatrix}$$

In using this method with the last test case the CPU time was reduced of around 60%. This result is logical because the number of bodies was divided by three.

4 Lowering or lifting a payload

In the last section, the unstretched length of each cable element was kept constant during the simulation. In case of lowering or lifting a payload, the length of the cable becomes variable. This effect has to be incorporated. Following [16] and [17], a method to do so is to modify the unstretched length of the first cable element:

$$Lu_1^t = Lu_1^{t-dt} + v.dt \quad (11)$$

Where Lu_1^t is the unstretched length of the first cable element at time t, v is the constant lowering velocity, positive for a lowering operation, negative for a lifting operation and dt is the time step.

This has an impact on the internal loads of the first cable element:

$$\Gamma_3 = \begin{cases} -\dfrac{EA}{Lu_1^t}(q_3 + Lu_1^t) - \dfrac{CA}{Lu_1^t}(\dot{q}_3 + v), & |q_3| \geq Lu_1^t \\ -\dfrac{CA}{Lu_1^t}(\dot{q}_3 + v), & |q_3| < Lu_1^t \end{cases} \quad (12)$$

During an operation of lowering, respectively lifting, when the length of the first element is too long, respectively too short, this first element is divided into two new elements, respectively the first element is merged with the second one. That involves adding, respectively deleting, one element in the cable. The criterion on the length of the first cable element is:

$$Lu_1 = \alpha.Lu \quad (13)$$

A value of 1.5 is chosen for α in case of lowering operations, 0.5 for the lifting operations.

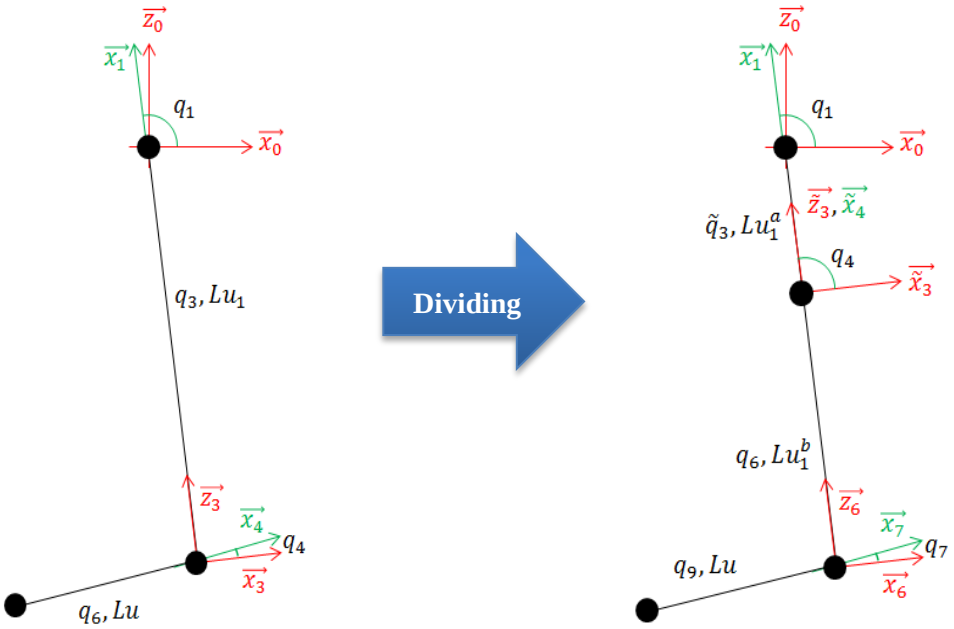

Figure 3: Sketch of the addition of a new cable element

5 Weak-scatterer theory and coupling with the multibody theory

In case of a lowering or lifting operation, a payload goes through the free surface. Thus the submerged part of the payload is deeply modified and some unsteady effects due to the hydrodynamic interaction between the ship and the payload appear. These phenomena prevent the use of a classical 1st order linear potential flow solver, this method being limited to the hypothesis of small amplitude motions. Regarding the second order linear potential flow approximation, the second order terms are taken into account but the free surface boundary equations stay written on $z = 0$. The small amplitude motion hypothesis has still to be valid.

Letournel [18] has developed a potential flow solver based on the weak-scatterer hypothesis for submerged bodies. Doing so, the velocity potential and the free surface elevation are splitted into two parts the incident and the scattered (perturbation) components:

$$\begin{aligned} \phi &= \phi_{incident} + \phi_{pertubation} \\ \eta &= \eta_{incident} + \eta_{perturbation} \end{aligned} \tag{14}$$

The weak-scatterer hypothesis assumes the perturbation part is small compared to the incident one.

$$\begin{aligned} \phi_{incident} &\ll \phi_{pertubation} \\ \eta_{incident} &\ll \eta_{pertubation} \end{aligned} \tag{15}$$

The free surface boundary conditions are linearized on the incident wave elevation. There is no condition on the amplitude of the motion of the floater, while the body condition is written on its exact position (Body exact approximation). This numerical tool has been extended to piercing bodies by Chauvigné [19].

As explained in [18] and [19], in case of a free body motion, the time-differentiation of the velocity potential is unknown. This quantity is computed from a second boundary value problem (*BVP*) in using the implicit condition method. The second *BVP* is constituted of three equations:

- The integral equation (Laplace equation on the velocity potential);
- The body condition (slip condition on the surface of the body);
- The motion equation.

To simulate a marine operation, the mechanical solver and the hydrodynamic solver has to be coupled. Different coupling strategies are available. Jonkman [20] and Yvin [21] listed the important families of coupling strategies.

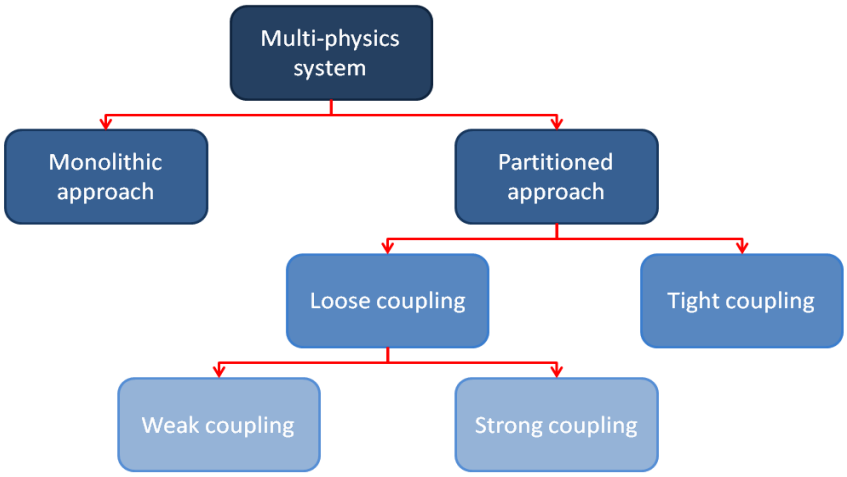

Figure 4: Different coupling methods

Monolithic approach is present when the code is made of one piece, with only one single equation representing the system, one time integrator and one spatial mesh. Otherwise, when the system can be decomposed into several subsystems with input-output relationship, it is a partitioned approach. A tight coupling is obtained when only one equation of motion represents all the subsystems (coupling equation). A loose coupling is present when each subprogram has its own time-stepper.
The mechanical solver and the hydrodynamic solver presented above are independent so a monolithic approach cannot be chosen. Contrary to a loose coupling, with a tight coupling, all quantities are time-stepped synchronously. This fact ensures the robustness and the accuracy of the coupling strategy and therefore larger time steps can be used. Thus a tight coupling is selected.

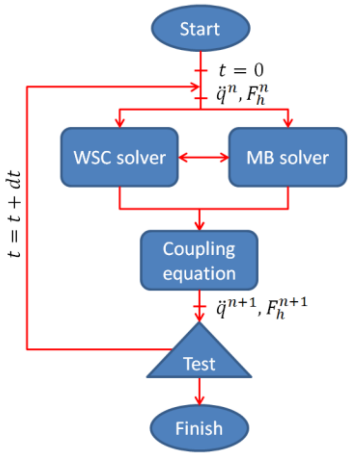

Figure 5: Tight partitioned approach for the coupling of the weak-scatterer code with InWave

In coupling the weak scatterer code with the multibody solver (represented by the equation (1)), modifications appear on both the body condition and the motion equation of the second *BVP*. The coupling equation will be exposed in case of a single floater considered as the base of the multibody system.

The hydrodynamic force ${}^{e}\boldsymbol{F}_0^{WSC}$ in the inertial frame is obtained by discretization of the Bernoulli equation:

$$ {}^{e}\boldsymbol{F}_0^{WSC} = {}^{e}\boldsymbol{CT}_0\boldsymbol{\phi}_t(B_0) + {}^{e}\boldsymbol{T}_0^{h} \tag{16} $$

Where $\boldsymbol{\phi}_t(B_0)$ is the time-differentiation of the velocity potential on the body surface, ${}^{e}\boldsymbol{CT}_0$ and ${}^{e}\boldsymbol{T}_0^{h}$ represent the other discretized terms of the Bernoulli equation.
In the multibody motion equation is written in the frame of each body, consequently equation (16) has to be written in the frame of the base.

$$ {}^{0}\boldsymbol{F}_0^{WSC} = \begin{pmatrix} {}^{0}\boldsymbol{R}_e & \boldsymbol{0_{3\times3}} \\ \boldsymbol{0_{3\times3}} & {}^{0}\boldsymbol{R}_e \end{pmatrix} {}^{e}\boldsymbol{F}_j^{WSC} \tag{17} $$

Where ${}^{0}\boldsymbol{R}_e$ is the rotation matrix between the inertial frame and the base frame.
Finally the Newton's second law for the multibody system is:

$$ \begin{pmatrix} \boldsymbol{0_{6\times1}} \\ \boldsymbol{\Gamma} \end{pmatrix} = \begin{pmatrix} \boldsymbol{H_{11}} & \boldsymbol{H_{12}} \\ \boldsymbol{H_{21}} & \boldsymbol{H_{22}} \end{pmatrix} \begin{pmatrix} {}^{0}\dot{\boldsymbol{V}}_0 \\ \ddot{\mathbf{q}} \end{pmatrix} + \begin{pmatrix} \boldsymbol{C_1} \\ \boldsymbol{C_2} \end{pmatrix} - \begin{pmatrix} {}^{0}\boldsymbol{F}_0^{WSC} \\ \boldsymbol{0_{nJoints\times1}} \end{pmatrix} \tag{18} $$

The body condition is:

$$ \boldsymbol{\phi}_{tn}(B_0) = \boldsymbol{CK}_0.\ddot{\boldsymbol{\eta}}_0 + \boldsymbol{Q}'_0 \tag{19} $$

Where $\boldsymbol{\phi}_{tn}(B_0)$ is the normal derivative of $\boldsymbol{\phi}_t(B_0)$, $\ddot{\boldsymbol{\eta}}_0$ is the acceleration of the base in the inertial frame, $\boldsymbol{CK}_0$ and $\boldsymbol{Q}'_0$ are the discretized terms of the body condition.

According to the equation (1), it is necessary to express $\ddot{\boldsymbol{\eta}}_0$ in function of ${}^{0}\dot{\boldsymbol{V}}_0$. As explained in [7] there is:

$$ \dot{\boldsymbol{\eta}}_0 = {}^{e}\boldsymbol{J}_0\boldsymbol{\nu} \tag{20} $$

With ${}^{e}\boldsymbol{J}_0$ the transformation matrix between $\dot{\boldsymbol{\eta}}_0$ and $\boldsymbol{\nu}$.
So the time-differentiation of this relation becomes:

$$ \ddot{\boldsymbol{\eta}}_0 = {}^{e}\dot{\boldsymbol{J}}_0\boldsymbol{\nu} + {}^{e}\boldsymbol{J}_0\dot{\boldsymbol{\nu}} \tag{21} $$

From [5] there is also:

$$ \dot{\boldsymbol{\nu}} = {}^{0}\dot{\boldsymbol{V}}_0 - \begin{pmatrix} S({}^{0}\boldsymbol{\omega}_0){}^{0}\boldsymbol{v}_0 \\ \boldsymbol{0_{3\times1}} \end{pmatrix} \tag{22} $$

Where S is the vector product matrix such as $S(\boldsymbol{u})\boldsymbol{v} = \boldsymbol{u}\times\boldsymbol{v}$, ${}^{0}\boldsymbol{\omega}_0$ and ${}^{0}\boldsymbol{v}_0$ are the angular and linear velocities of the body in the frame of the body.

Hence:

$$ \boldsymbol{\phi}_{tn}(B_0) = \boldsymbol{CK}_0.{}^{e}\boldsymbol{J}_0{}^{0}\dot{\boldsymbol{V}}_0 + \boldsymbol{CK}_0.\left[{}^{e}\dot{\boldsymbol{J}}_0\nu - {}^{e}\boldsymbol{J}_0\begin{pmatrix} S({}^{0}\boldsymbol{\omega}_0){}^{0}\boldsymbol{v}_0 \\ \boldsymbol{0_{3\times1}} \end{pmatrix}\right] + \boldsymbol{Q}'_0 \tag{23} $$

The integral equation is unchanged:

$$ \boldsymbol{CS}(:,FS).\boldsymbol{\phi}_{tn}(FS) - \boldsymbol{CD}(:,B_0)\boldsymbol{\phi}_t(B_0) - \boldsymbol{CD}(:,Ext)\boldsymbol{\phi}_t(Ext) + \boldsymbol{CS}(:,B_0)\boldsymbol{\phi}_t(B_0) = \boldsymbol{CD}(:,FS)\boldsymbol{\phi}_t(FS) - \boldsymbol{CS}(:,Ext)\boldsymbol{\phi}_{tn}(Ext) \tag{24} $$

Where CS and CD are the matrices of the influence coefficients. FS, B_0 and Ext represents the part of the influence coefficient or $\boldsymbol{\phi}_t$ or $\boldsymbol{\phi}_{tn}$ dedicated to the free surface, the floater and the tank.

The final system or coupling equation is $\boldsymbol{AX} = \boldsymbol{B}$ with:

$$\boldsymbol{A} = \begin{pmatrix} \boldsymbol{CS}(:,FS) & -\boldsymbol{CD}(:,B_0) & -\boldsymbol{CD}(:,B_{Ext}) & \boldsymbol{CS}(:,B_0) & \boldsymbol{0}_{N\times 6} & \boldsymbol{0}_{N\times n} \\ \boldsymbol{0}_{Nb\times NFS} & \boldsymbol{0}_{Nb\times Nb} & \boldsymbol{0}_{Nb\times NExt} & \boldsymbol{I}_{Nb} & -\boldsymbol{CK}_0\,{}^e\boldsymbol{J}_0 & \boldsymbol{0}_{Nb\times n} \\ \boldsymbol{0}_{6\times NFS} & -{}^0\boldsymbol{CT}_0 & \boldsymbol{0}_{6\times NExt} & \boldsymbol{0}_{6\times Nb} & \boldsymbol{H}_{11} & \boldsymbol{H}_{12} \\ \boldsymbol{0}_{n\times NFS} & \boldsymbol{0}_{n\times Nb} & \boldsymbol{0}_{n\times NExt} & \boldsymbol{0}_{n\times Nb} & \boldsymbol{H}_{21} & \boldsymbol{H}_{22} \end{pmatrix}$$

$$\boldsymbol{B} = \begin{pmatrix} \boldsymbol{CD}(:,FS)\phi_t(FS) - \boldsymbol{CS}(:,Ext)\phi_{tn}(\boldsymbol{Ext}) \\ \boldsymbol{CK}_0\left[{}^e\dot{\boldsymbol{J}}_0\boldsymbol{v} - {}^e\boldsymbol{J}_0\begin{pmatrix} S({}^0\boldsymbol{\omega}_0)\,{}^0\boldsymbol{v}_0 \\ 0_{3\times 1}\end{pmatrix}\right] + \boldsymbol{Q'}_0 \\ -\boldsymbol{C}_1 + {}^0\boldsymbol{T}_0{}^h \\ \boldsymbol{\Gamma} - \boldsymbol{C2} \end{pmatrix} \qquad \boldsymbol{X} = \begin{pmatrix} \phi_{tn}(FS) \\ \phi_t(B_0) \\ \phi_t(Ext) \\ \phi_{tn}(B_0) \\ {}^0\dot{\boldsymbol{V}}_0 \\ \ddot{\boldsymbol{q}} \end{pmatrix}$$

With N the total number of nodes in the mesh, N_{ext} the number of nodes for the tank and N_{FS} the number of nodes for the free surface.

This coupling equation would stay the same in case of a fully non-linear potential flow solver.

6 Numerical results

6.1 Coupling verification on a WEC test case

This coupling is applied to simulate the motion of a wave energy converter (*WEC*) of type CETO. It is a sphere of radius 3.5 m, the position of the center of gravity is 7 m below the free surface and the water depth is 20 m. The mass of the sphere is its displacement. The power take-off is made of a spring-damper system. The stiffness of the spring is 302478.6 $N.m^{-1}$, the unstretched length is 13 m and the damping coefficient is 50 000 $kg.s^{-1}$. The sphere can only move in heave. The incident wave is a regular wave of amplitude 1.25 m and wave frequency 1.0 $rad.s^{-1}$.

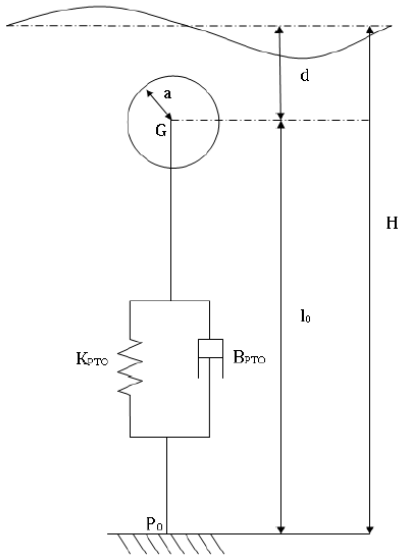

Figure 6: Sketch of a CETO system

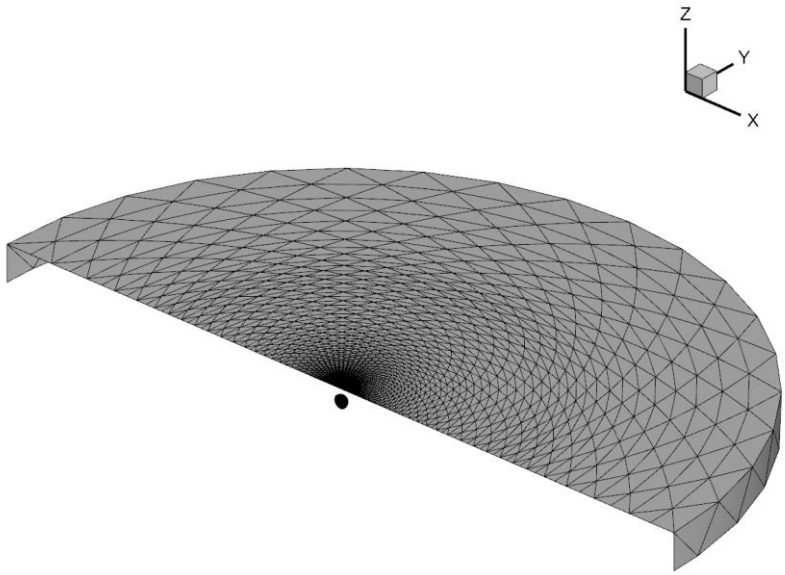

Figure 7: Mesh of the tank, the free surface and the sphere.

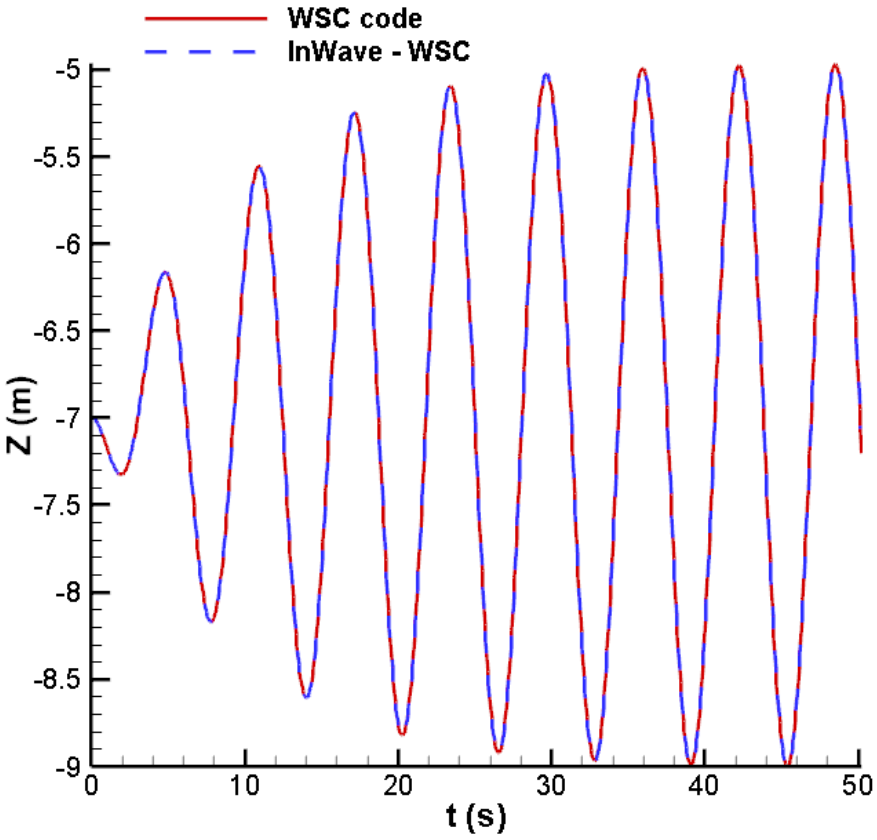

Figure 8: Comparison of the heave motion for the WSC code and the coupling InWave-WSC

The figure 9 shows the responses of the coupling, between InWave and the weak-scatterer, and the weak-scatterer code only are the same.

6.2 Academic test case: a floater, a cable and a payload

This coupling is now applied on an academic test case with a floater, a cable and a payload. A floating cylinder of radius 0.2 m and length 1 m only moves in surge and is linked to the center of the tank by a spring of stiffness 1990 $N.m^{-1}$. The mass of the cylinder is 64.4 kg. A crane is fixed to this floater with, at the other extremity, a cable made of 3 elements. The Young modulus is 77.5e6 Pa, the damping coefficient is 100 Pa.s, the cable linear density is 2 $kg.m^{-1}$, and the unstretched length of each element is 0.5 m. At the extremity of the cable free to move, an extra mass of 5 kg is added (payload). Thus the total mass of the system is 74.5 kg. At t = 0 s the cable is vertical at the equilibrium. This equilibrium was obtained in using the multibody solver presented in 3.

Element	Size (m)
1 (crane)	0.50073
2	0.50058
3 (payload)	0.50044

Table 2: Size of each cable element at t = 0 s

A regular wave of amplitude 0.05 m and wave frequency 3.14 $rad.s^{-1}$ is generated.

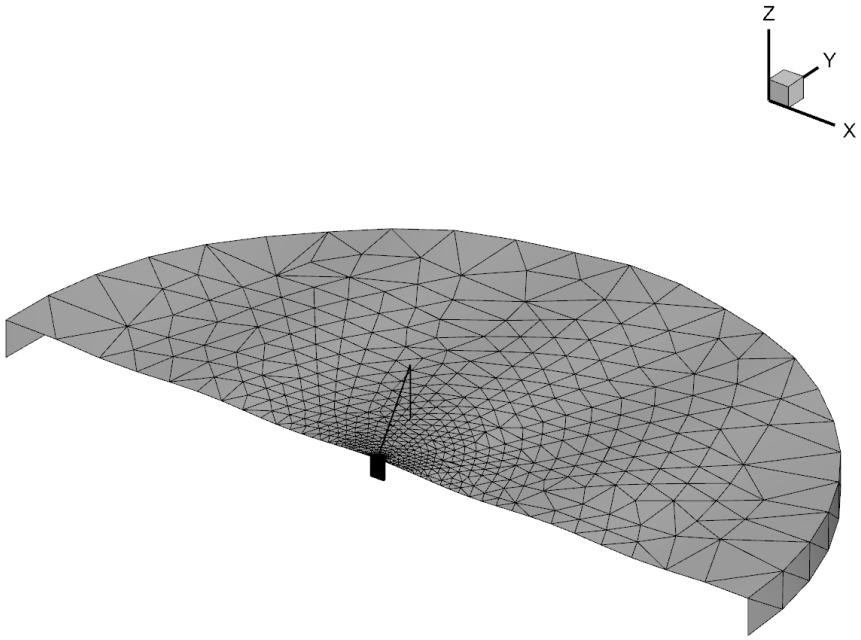

Figure 9: Mesh of the tank, the free surface, the floater and the cable

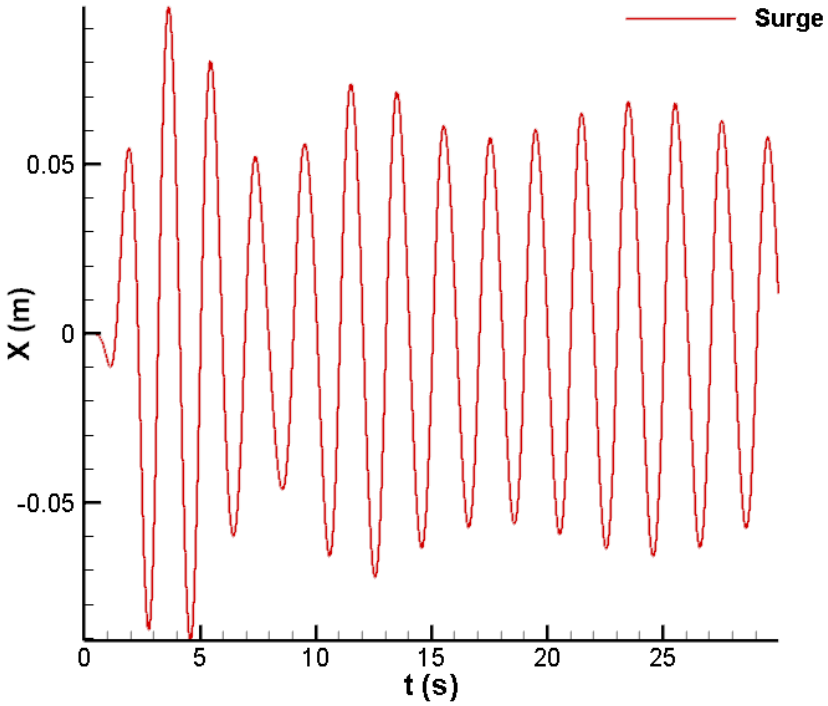

Figure 10: Surge motion of the cylinder

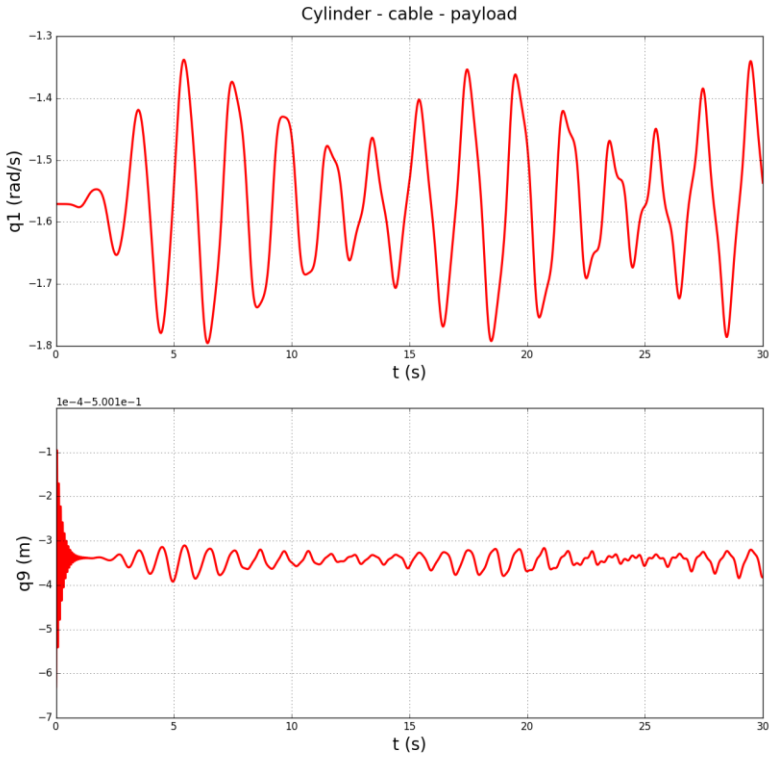

Figure 11: Rotation of the first cable element with respect to the crane (top) and length of the third element (bottom)

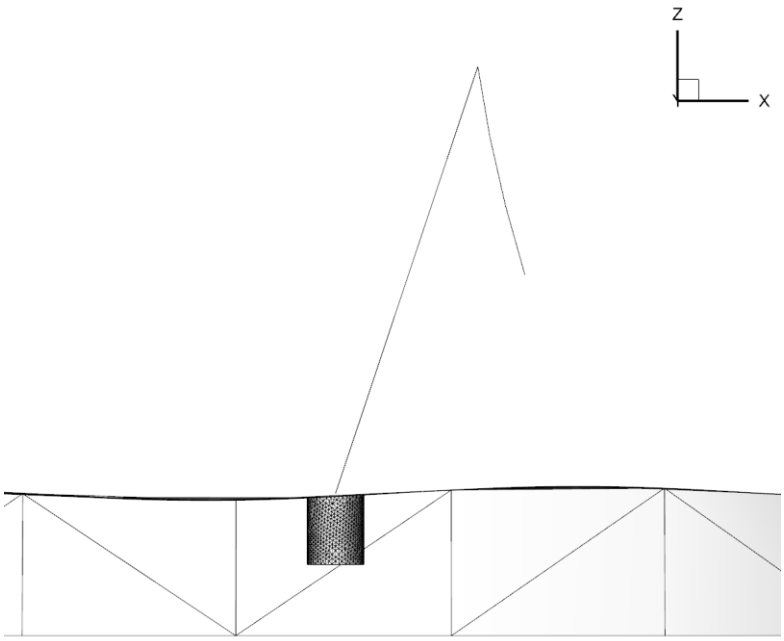

Figure 12: Mesh at t = 20.64 s

Thus, the hydrodynamic loads on the floater are propagated from the cylinder to the cable and the payload and generate their motion. In return, the presence of the cable and the payload modifies the motion of the cylinder.

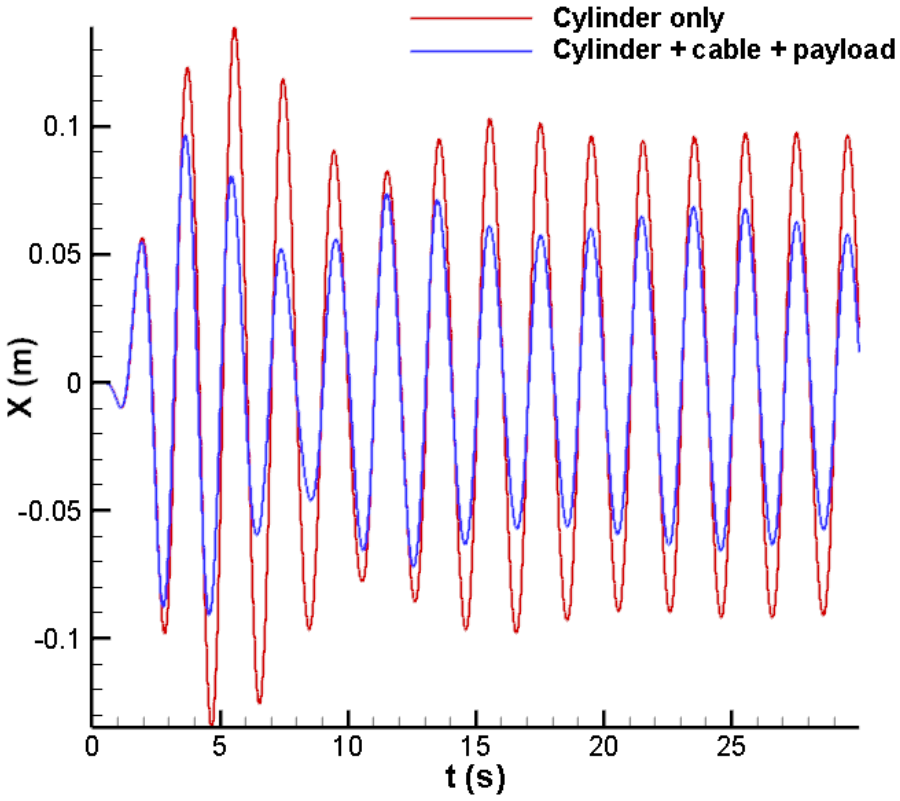

Figure 13: Motion of the cylinder only (red) and the cylinder + the cable + the payload (blue)

On the figure 13, the surge motion of the whole system (cylinder, cable and the payload) is plotted with the motion of the cylinder only with the same total mass (74.5 kg). Thus the presence of the cable and the payload decreases the amplitude of the motion of the cylinder. The frequency of the response stays the same in the both cases.

7 Conclusion

In this paper, a new approach for the numerical simulation of the lifting and lowering operations was presented. It is based on the development and the adaptation of the Composite Rigid Body Algorithm for the mechanical solver and on a potential flow hypothesis with a weak-scatterer approximation for the hydrodynamic solver. The cable is simulated with the multibody solver. Attention is paid to the cable formalism to reduce the number of iterations and thus computation time. Finally the two solvers are coupled with a tight coupling strategy. A test case with a CETO wave energy converter has proved the validity of the coupling equation presented. An academic test case of a marine operation with a floater, a cable and a payload has been done.

This coupling needs to be deeply validated and extended to the cases where the floater is not at the root of the multibody system and when there are several floaters. The interest of the weak-scatterer approach has to be quantified in comparison to the numerical tools using a classical linear potential flow solver.

References

[1] DNV-RP-H103, Modelling and analysis of marine operations, DNV, 2011.
[2] https://www.orcina.com/SoftwareProducts/OrcaFlex/
[3] http://www.principia-group.com/
[4] M. Hannan, Numerical simulation of submerged payload coupled with crane barge in waves, PhD thesis, 2014.
[5] A. Combourieu, M. Philippe, F. Rongère, A. Babarit, *InWave*: A new flexible design tool dedicated to wave energy converters, Proceedings of the ASME 2014 33rd International Conference on ocean, Offshore and Artic Engineering, June 2014, San Francisco, United States.
[6] W. Khalil, J. F. Kleinfinger, A new geometric notation for open and closed-loop robots, Proceedings of the 1986 IEEE International Conference on Robotics and Automation, 1986, pp. 1174-1179.
[7] F. Rongère, A. Clément, Systematic dynamic modeling and simulation of multibody offshore structures: application to wave energy converters, Proceedings of the ASME 2013 32rd International Conference on ocean, Offshore and Artic Engineering, June 2013, Nantes, France.
[8] R. Featherstone, Rigid body dynamics algorithms, Springer-Verlag New Torc Inc, 2008.
[9] F. Rongère, Modèle dynamique des systèmes multicorps flottants avec prise en compte des interactions hydrodynamiques entre les corps *(in french)*, internal report, 2014.
[10] http://map-plus-plus.readthedocs.io
[11] http://www.matt-hall.ca/moordyn/
[12] M. Masciola, J. Jonkman, A. Robertson, Extending the capabilities of the mooring analysis program: a survey of dynamic mooring line theories for integration into FAST, Proceedings of the ASME 2014 33rd International Conference on ocean, Offshore and Artic Engineering, June 2014, San Francisco, United States.
[13] M. Masciola, J. Jonkman, A. Robertson, Implementation of a multisegmented, quasi static cable model, Proceedings of the ASME 2013 32rd International Conference on ocean, Offshore and Artic Engineering, June 2013, Nantes, France.
[14] B. Buckham, Dynamics modeling of low-tension tethers for submerged remotely operated vehicles, PhD thesis, 2003.
[15] M. Hall, A. Goupee, Validation of a lumped-mass mooring model with DeepCwind semisubmersible model test data, Ocean Engineering, Volume 104, August 2015, pp 590-603.
[16] OrcaFlex Manual (Version 9.1a), Orcina Ltd.
[17] S. Prabhakar, B. Buckham, Dynamics modeling and control of a variable length remotely operated vehicle tether, Proceedings of OCEANS 2005 MTS/IEEE, Washington, DC, Volume 2, 2005, pp. 1255-1262.
[18] L. Letournel, Développement d'un outil de simulation numérique basé sur l'approche weak-scaterer pour l'étude des systèmes houlomoteurs en grands mouvements *(in french)*, PhD thesis, 2015.
[19] C. Chauvigné, L. Letournel, A. Babarit, G. Ducrozet, P. Bozonnet, J-C. Gilloteaux, P. Ferrant, Progresses in the development of a weakly-nonlinear wave body interaction model based on the weak-scatterer approximation, Proceedings of the ASME 2015 34rd International Conference on ocean, Offshore and Artic Engineering, June 2014, St. John's, Newfoundland, Canada.
[20] J. Jonkman, The new modularization framework for the FAST wind turbine CAE tool, Proceedings of the 2013 51st AIAA Aerospace Sciences meeting including the New Horizons Forum and Aerospace Exposition, January 2013, Grapevine, Texas, United States.

[21] C. Yvin, Interaction fluide-structure pour des configurations multi-corps. Applications aux liaisons complexes, lois de commande d'actionneur et systèmes souples dans le domaine maritime (*in french*), PhD thesis, 2014.